Abstract

Apart from single gravitational wave (GW) events, those with a smaller amplitude produce a stochastic GW background. This has not been measured yet using traditional GW detectors, like the Laser Interferometer Gravitational-Wave Observatory (LIGO), Virgo or the Kamioka Gravitational Wave Detector (KAGRA). With future detectors, such as Einstein Telescope (ET) or Cosmic Explorer (CE), it is expected to be observed in the frequency range of $\approx 10 - 10^4$ Hz. The astrophysical gravitational wave background (AGWB) is modelled here in a frequency-dependent way using the `MultiCLASS` code. Then, we use Information Field Theory (IFT) to separate it from Gaussian instrumental noise in harmonic space as a proof of concept. *Results*

List of Abbreviations

AGWB	Astrophysical Gravitational Wave Background
BBH	Binary Black Hole
BH	Black Hole
CE	Cosmic Explorer
CGWB	Cosmological Gravitational Wave Background
CLASS	Cosmic Linear Anisotropy Solving System
ET	Einstein Telescope
GW	Gravitational Wave
GWTC	Gravitational Wave Transient Catalogue
HMF	Halo Mass Function
IFT	Information Field Theory
KAGRA	Kamioka Gravitational Wave Detector
LIGO	Laser Interferometer Gravitational-Wave Observatory
NANOGrav	North American Nanohertz Observatory for Gravitational Waves
NIFTy	Numerical Information Field TheorY
NS	Neutron Star
SFR	Star Formation Rate

Contents

1

Introduction

Most large-scale structure surveys, like Planck (todo cite planck), have found an unexpectedly large dipole anisotropy, which can be used to test the cosmological principle. The principle states that the universe is isotropic and homogeneous on large scales. These surveys have error sources, such as partial sky covering due to masking sources and the fact that clustering of matter can produce a dipole contribution.

Gravitational waves have a very high sky coverage since masking is not necessary for GW detectors. Thus, we can use GW observations to test the cosmological principle in an independent way. To do this, we can look at the astrophysical gravitational wave background (AGWB), specifically compact binary mergers. They are expected to make up the majority of the GW background. This background has been detected in a low-frequency range of $10^{-8.75} - 10^{-7.5}$ Hz.

Many GW have an amplitude below the necessary signal-to-noise ratio to be detected individually. These sources form the GW background. The first detection of this background was made in 2023 by the NANOGrav pulsar time array with an energy density parameter of $\Omega_{GW} = 9.3^{+5.8}_{-4.0} \cdot 10^{-9}$ Agazie et al. 2023. In current GW experiments, like LIGO, Virgo and KAGRA, the noise is too high to detect this background. Experiments with a higher sensitivity are planned for the future, like the ground-based Einstein Telescope (ET) and Cosmic Explorer (CE). These might have low enough noise to detect the GW background and even disentangle different components.

With new detectors in the future we could measure intrinsic anisotropies in this background which are not coming from our observer motion or statistical properties, so-called shot noise from a Poisson distribution. These anisotropies, like for example the dipole, would contradict the cosmological principle. It states that the universe is homogeneous and isotropic at every point.

We compute the anisotropies of the (AGWB) in a frequency-dependent way using a modified version of `CLASS`, an Einstein-Boltzmann solver. Then, we use a separation method from information field theory (IFT) on the AGWB at different frequencies, as well as on the cosmological GW background.

We find that the signal can be partly recovered for the AGWB at frequencies with a high angular power spectrum. However, for most frequencies of the AGWB, as well as for the cosmological background, the separation does not work.

2

Gravitational Waves

2.1 Fundamentals

GW are oscillations in spacetime, similar to electromagnetic waves. We can start with the Einstein equation:

$$G_{\mu\nu} = \frac{8\pi G}{c^4} T_{\mu\nu}. \tag{2.1}$$

Since GW (mostly) propagate in the vacuum and we assume a small amplitude $|\delta g_{\mu\nu}| \ll 1$, we arrive at the following differential equation.

$$T_{\mu\nu} = 0 \tag{2.2}$$

$$\Rightarrow G_{\mu\nu} = 0 \tag{2.3}$$

We assume that the metric only has small linear perturbations.

$$g_{\mu\nu}(t, \vec{x}) = \bar{g}_{\mu\nu}(t) + \delta g_{\mu\nu}(t, \bar{x}) \tag{2.4}$$

$$= \eta_{\mu\nu} + 2\kappa h_{\mu\nu} \tag{2.5}$$

$$\kappa = \frac{\sqrt{8\pi G}}{c^2} \approx 2.1 \cdot 10^{-41} \frac{\mathrm{s}^2}{\mathrm{kg\,m}} \tag{2.6}$$

$$|h_{\mu\nu}| << 1 \tag{2.7}$$

Here $\eta_{\mu\nu}$ the Minkowski metric for flat spacetime.

We can solve the differential equation with the trace reverse tensor.

$$\bar{h}_{\mu\nu} = h_{\mu\nu} - \frac{1}{2}\eta_{\mu\nu} h \tag{2.8}$$

Here, h is the trace of $h_{\mu\nu}$.

2.1.1 Wave Equation

If we want to describe the transport of energy and momentum by GW analytically, we can assume an asymptotically flat environment since the detector is at a far distance from the source. Then, we will consider Newtonian binaries in a circular orbit and only look at the non-relativistic regime. This will limit us to the inspiral phase, see Fig. 2.3 since the non-relativistic approximation only applies in that phase. Later though, we will see that for the implementation in the `CLASS` code all the phases need to be modelled.

The linear perturbation $h_{\mu\nu}$ is a dimensionless bosonic tensor field and thus follows the massless field equation (Holten 2019):

$$\Box h_{\mu\nu} - \partial_m u \partial^\lambda h_{\lambda\nu} - \partial_\nu \partial^\lambda h_{\lambda\mu} + \partial_\mu \partial_\nu h - \eta_{\mu\nu}(\Box h - \partial^\kappa \partial^\lambda h_{\kappa\lambda}) = -\kappa T_{\mu\nu} \tag{2.9}$$

For the gauge transformation, we can impose the de Donder gauge condition:

$$\partial^\mu h_{\mu\nu} = \frac{1}{2}\partial_\nu h^\mu_\mu. \tag{2.10}$$

This simplifies the wave equation to the following form with the trace reverse tensor (2.8).

$$\partial^\mu \underline{h}_{\mu\nu} = 0 \tag{2.11}$$

$$\Rightarrow \Box \underline{h}_{\mu\nu} = -\kappa T_{\mu\nu} \tag{2.12}$$

We can also choose h to be traceless, which leads to h and $\underline{h}$ coinciding.

$$h = h^\mu{}_\mu := 0 \tag{2.13}$$

$$\Rightarrow \underline{h}_{\mu\nu} = h_{\mu\nu} \tag{2.14}$$

$$\Rightarrow \underline{h} = \underline{h}^\mu{}_\mu = 0 \tag{2.15}$$

2.1.2 Free Field Modes

Now, we can perform a Fourier decomposition of the linear perturbation.

$$\underline{h}_{\mu\nu}(x) = \int \frac{d^4k}{(2\pi)^2} \epsilon_{\mu\nu}(k) e^{-ikx} \tag{2.16}$$

$$k = (\omega, \vec{k}) \tag{2.17}$$

The field equation is invariant under the following gauge transformation.

$$\epsilon'_{\mu\nu} = \epsilon_{\mu\nu} + k_\mu \alpha_\nu + k_\nu \alpha_\mu - \eta_{\mu\nu} k^\lambda \alpha_\lambda \tag{2.18}$$

Since k is the wave vector and GW propagate with the speed of light, it has to be a light-like four-vector.

$$k^2 = 0 \tag{2.19}$$

$$\Rightarrow \epsilon_{\mu\nu}(k) = e_{\mu\nu}(k)\delta(k^2) \tag{2.20}$$

To get a simplified amplitude form, we choose α from the gauge condition 2.18 in such a way that we eliminate e'_{00}, e'_{i0} and e'_{ii}.

$$\epsilon'_{\mu\nu}(k) = e'_{\mu\nu}(k)\delta(k^2) \tag{2.21}$$

For a wave propagating in z-direction, we will then get the following amplitude form.

$$e'_{\mu\nu}(\omega,\vec{k}) = \begin{pmatrix} 0 & 0 & 0 & 0 \\ 0 & e_+(\omega) & e_\times(\omega) & 0 \\ 0 & e_\times(\omega) & -e_+(\omega) & 0 \\ 0 & 0 & 0 & 0 \end{pmatrix} \tag{2.22}$$

To illustrate plus and cross polarisations, Fig. 2.1 shows both over one period.

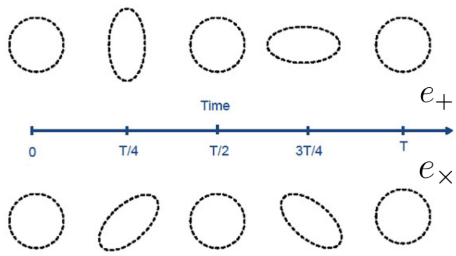

Figure 2.1: Illustration of the plus and cross polarisations varying with time. The figure is taken from a lecture by Prof. Jan van Holten.

Then, a plane wave in z-direction with plus polarisation would have the following expression, since the cross polarisation will be zero.

$$h(z,t) = h_+ \begin{pmatrix} 0 & 0 & 0 & 0 \\ 0 & 1 & 0 & 0 \\ 0 & 0 & -1 & 0 \\ 0 & 0 & 0 & 0 \end{pmatrix} e^{i(kz-\omega t)} \tag{2.23}$$

For a length of L_0 along the x-axis, it would oscillate in size in the following way:

$$L(t) = L_0 + \frac{h_+ L_0}{2} cos(\omega t). \tag{2.24}$$

2.1.3 Quadrupole Wave Emission

If we have a source in a finite region of space, we can use the retardated Green's function to solve the wave equation. This is because the waves are causally related to the source $t > |\vec{x}' - \vec{x}|$.

$$\Box \underline{h}_{\mu\nu} = -\kappa T_{\mu\nu} \tag{2.25}$$

$$\Rightarrow \underline{h}_{\mu\nu}(\vec{x},t) = \frac{\kappa}{4\pi} \int d^3x' \frac{T_{\mu\nu}(\vec{x}', t - |\vec{x}' - \vec{x}|)}{|\vec{x}' - \vec{x}|} \tag{2.26}$$

Then, we can assume that we are in the far field regime, such that $|\vec{x}| \gg |\vec{x}'|$.

$$r := |\vec{x}| \approx |\vec{x}' - \vec{x}| \tag{2.27}$$

$$\Rightarrow \underline{h}_{\mu\nu}(\vec{x},t) = \frac{\kappa}{4\pi r} \int d^3x' T_{\mu\nu}(\vec{x}', t - r) \tag{2.28}$$

If we consider a localised source, the solution does not have a dynamical time component, i.e. $\partial_0 h_{0j} = 0$ (Holten 2019). Additionally to the de Donder gauge (2.10), we will now impose the traceless-transverse (TT) gauge, which implies transversality.

$$r_i \underline{h}_{ij} = 0 \tag{2.29}$$

$$h_{ii} = 0 \tag{2.30}$$

This gives us the following solution which is valid at a large distance in empty space.

$$\underline{h}_{ij}(\vec{x}, t) = \frac{\kappa}{4\pi}(\delta_{ik} - \hat{r}_i \hat{r}_k)(\delta_{jl} - \hat{r}_j \hat{r}_l)\left(I_{kl} + \frac{1}{2}\delta_{kl}\vec{r}\ \underline{I}\ \vec{r}\right) \tag{2.31}$$

I_{ij} is the quadrupole moment of the total energy density:

$$I_{ij}(t-r) = \int d^3x' \left(T_{ij} - \frac{1}{3}\delta_{ij}T_{kk}\right) T_{00}(\vec{x}', t-r). \tag{2.32}$$

$$= \frac{1}{2}\partial_0^2 \int d^3x' \left(x'_i x'_j - \frac{1}{3}\delta_{ij}\vec{x}'^2\right) T_{00}(\vec{x}', t-r). \tag{2.33}$$

The last equation follows since the time derivative is equal to the derivative with respect to the retardated time $u = t - r$.

$$\partial_0 = \partial_u \tag{2.34}$$

$$\Rightarrow \partial_0^2 T_{00}(\vec{x}', u) = \partial_0 \partial'_i T_{i0}(\vec{x}', u) = \partial'_i \partial'_j T_{ij}(\vec{x}', u) \tag{2.35}$$

As mentioned earlier, we can perform a non-relativistic approximation for the inspiral phase. In this case, the energy density is dominated by the mass density. We can thus rewrite $\underline{h}_{ij}$ with the mass quadrupole moment.

$$I_{ij} = \frac{1}{2}\frac{\partial^2 Q_{ij}}{\partial t^2} \tag{2.36}$$

$$Q_{ij}(t-r) = \frac{1}{2}\int d^3x' \left(x'_i x'_j - \frac{1}{3}\delta_{ij}\vec{x}'^2\right) \rho(\vec{x}', t-r) \tag{2.37}$$

GW cannot form from a dipole mass distribution since that would require negative masses. However, if we have a quadrupole distribution with vacuum and masses (like a binary black hole for example), GW can be created.

The wave field for non-relativistic sources is thus:

$$\underline{h}_{ij}(\vec{x}, t) = \frac{\kappa}{8\pi}(\delta_{ik} - \hat{r}_i \hat{r}_k)(\delta_{jl} - \hat{r}_j \hat{r}_l)\frac{\partial^2}{\partial t^2}\left(Q_{kl} + \frac{1}{2}\delta_{kl}\vec{r}\ \underline{Q}\ \vec{r}\right) \tag{2.38}$$

2.2 Stochastic Background

The stochastic GW background consists of all sources that are too faint to be resolved individually, thus it is a superposition of many independent sources. The same source can contribute to multiple frequencies over time. The biggest background comes from astrophysical sources, like compact object mergers, but there is also a smaller cosmological background present. That one originates from early universe phenomena. To measure the background we need the correlation between two detector outputs Christensen 2019. If the noise between them is uncorrelated, it will average out over time and leave the background signal.

$$\langle s_1(t)s_2(t)\rangle \ = \ \langle (n_1(t) + h(t))(n_2(t) + h(t))\rangle \tag{2.39}$$

$$= \langle n_1(t)n_2(t)\rangle + \langle n_1(t)h(t)\rangle + \langle h(t)n_2(t)\rangle + \langle h(t)h(t)\rangle \tag{2.40}$$

$$\approx \langle h(t)h(t)\rangle \tag{2.41}$$

From there we can compute the root mean square of the strain.

$$h_{rms}^2 = \langle \sum_{i,j} h_{ij}h_{ij}\rangle \tag{2.42}$$

$$= \int_0^\infty df\, S_h(f) \tag{2.43}$$

Here S_h is the spectral density, from which we can derive the GW energy density.

$$\rho_{GW} = \int_0^\infty df\, S_h(f)\frac{\pi c^2 f^2}{8G} \tag{2.44}$$

The frequency-dependent monopole depends on this energy density. Here, we consider the observed frequency f_o.

$$\bar{\Omega}_{AGWB}(f_o) = \frac{d\rho_{GW}}{df} \tag{2.45}$$

The energy density parameter is the frequency-dependent monopole integrated over the logarithmic frequency.

$$\Omega_{GW} = \int d\ln f\, \Omega_{GW}(f_o) \tag{2.46}$$

$$\approx \int d\ln f\, \bar{\Omega}_{AGWB}(f_o) \tag{2.47}$$

2.2.1 Astrophysical

GW can be created by different sources. Considering astrophysical sources, they can come from merging binaries, bursts (e.g. from core-collapse supernovae) or continuous waves (e.g. from pulsars). The AGWB consists mostly of compact object mergers, which are mainly black holes and neutron stars.

Anisotropy limits from LIGO: (check for more current) The LIGO anisotropy limit for the first observing run O1 published in 2017 was

$$\Omega_{2/3} = (4.4 \pm 6.4) \cdot 10^{-8}. \tag{2.48}$$

This is compatible with zero, but an anisotropic background would indicate a more interesting cosmology, which is why it would be important to disentangle any anisotropic that could be observed.

The AGWB was detected for the first time this year (2023) using the pulsar time array NANOGrav Agazie et al. 2023. Pulsar time arrays use the fact that pulsars are very accurate clocks. They are rotating neutron stars that have a strong magnetic field and thus emit radio waves in very regular intervals. Since they are so stable, we can use these signals as accurate clocks. If there are any changes in the time of arrival of multiple pulsars, this could indicate a GW background. The NANOGrav experiment used a frequency range of $10^{-8.75} - 10^{-7.5}$ Hz. They assumed a GW energy density parameter proportional to $f^{-2/3}$, which is the case in the inspiral phase of binary black holes. Phinney 2001 Using this, they find an integrated energy density $\Omega_{GW} = 9.3^{+5.8}_{-4.0} \cdot 10^{-9}$.

Binary Black Hole Mergers

A compact binary coalescence will produce a chirp-like GW signal, like in 2.3. Both massive objects attract each other and decrease their orbit around each other in the inspiral phase. The potential energy is converted into a GW. After the inspiral phase, the merger and ringdown phases follow, where the new BH becomes axisymmetric and stops emitting GW. The frequency increases over time during all three phases.

The inspiral phase is the simplest to describe analytically, see 2.1. However, in this work, we consider all three phases of the GW. We will see later that this is necessary to derive a frequency dependence.

In this work, we focus on binary black holes. Since most resolved events from LIGO/Virgo are binary black holes. In a recent analysis of the Gravitational Wave Transient Catalogue 3 (GWTC-3) by Collaboration et al. 2022, they considered events with a false alarm rate of less than $\frac{1}{4}$ per year. Out of this sample of 67 events, 63 came from binary black holes, 2 from binary neutron stars and 2 from neutron star-black hole mergers.

If we consider the energy density parameter of the stochastic GW background, we see that binary black holes are present at frequencies up to around 1000 Hz, see Fig. 2.2.

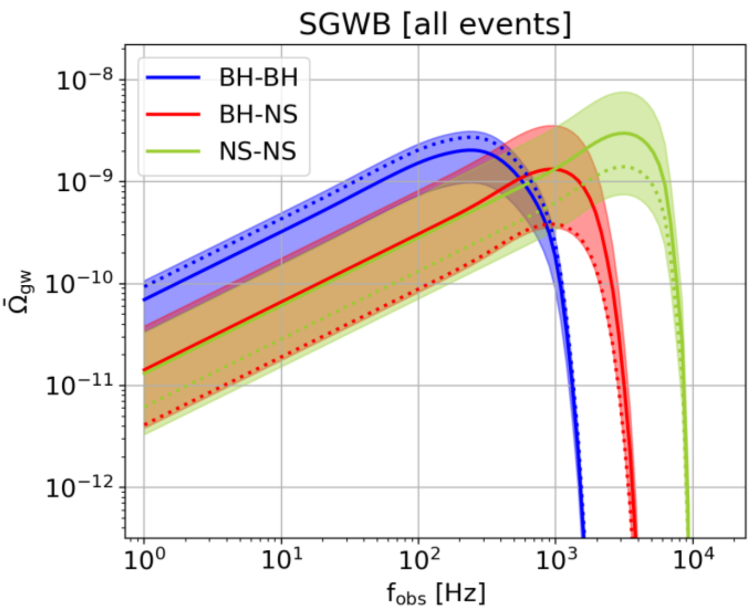

Figure 2.2: The GW energy density parameter as a function of frequency from 1 to 10,000 Hz. This shows the different contributions from BH-BH, NS-NS and BH-NS events. All curves are normalised to the local advanced LIGO/Virgo merger rate. The Figure is taken from Ref. Capurri et al. 2021.

In this figure, all three curves are normalised to the local merger rate from the advanced LIGO/Virgo detectors. Without this normalisation binary BH mergers dominate at most frequencies at which they are present. We can see that for the frequency range of $1-1000Hz$, it is reasonable to only consider BBH in our analysis since they are the most present source. However, the applied formalism for the frequency dependence can be generalised to a system of a BH and a neutron star or a system of two neutron stars.

From the waveform, we can extrapolate black hole properties, like the chirp mass and the spin.

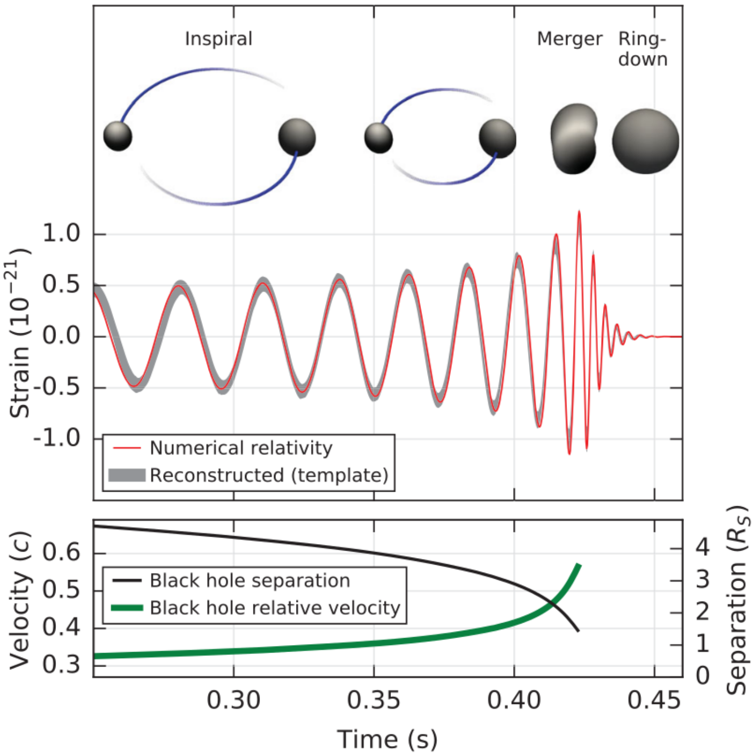

Figure 2.3: The different stages of a BBH merger with the corresponding waveform, here an illustrative estimate of GW150914. The Figure is taken from Ref. Abbott et al. 2016.

$$\mathcal{M}_c = \frac{(m_1 m_2)^{3/5}}{(m_1 + m_2)^{1/5}} \tag{2.49}$$

The frequency is determined by the total mass. The waveform can be decomposed into harmonic, where the quadrupole ($(\ell, m) = (2, 2)$) is naturally the dominant one. (insert from Bonn lectures?)

Dipole

The cosmological principle says, that the universe is isotropic and homogeneous on large scales. GW are one mode of testing this further. If we find anisotropies in the GW background, other than the kinematic dipole and shot noise, this would be evidence against the principle. The kinematic dipole arises from the observer motion with respect to the large-scale structure rest frame. More GW events should be detected in the direction in which we move, and fewer in the opposite direction. Shot noise comes from stochastic fluctuations in the background, which follow a Poisson distribution.

The GW density contrast can be written with an integration over the window function, which weights the contributions in the redshift domain.

$$\delta(f_0, \hat{n}) = \frac{\Omega(f_0, \hat{n}) - \overline{\Omega}(f_0)}{\overline{\Omega}(f_0)} \tag{2.50}$$

$$= \int dz\, W(f_0, z)\, \Delta(f_0, \hat{n}, z) \tag{2.51}$$

2.2.2 Cosmological

The major contributions to the cosmological GW background are primordial black holes and GW from phase transitions and inflation. Schulze et al. Schulze et al. 2023 computed the angular power spectrum of this background using a modified version of CLASS Blas, Lesgourgues, and Tram 2011 called `GW_CLASS`. Bubbles of a phase can form in a universe which is in an older phase. In there, magnetohydrodynamic (MHD) turbulence can also produce GW. TODO: PBH shortly Using this code, one can choose a source of this background and compute the associated angular power spectrum. Here, we use the signal from the expected inflationary GW background with a blue tilt. So, we will have a stronger background at higher frequencies compared to lower frequencies.

Inflation

A period of inflation in the early universe solves two important cosmological problems, namely the flatness and the horizon problem. The flatness problem arises when we assume radiation domination followed by matter domination which is followed by Λ (the cosmological constant) domination. The spatial curvature density parameter is measured to be very low.

$$|\Omega_k| = \frac{\rho_k^{\text{eff}}}{\rho_{crit}} < 10^{-2} \tag{2.52}$$

On the other hand, the radiation energy density parameter is of an even lower order.

$$|\Omega_r| = \frac{\rho_r}{\rho_{crit}} \in \mathcal{O}(10^{-4}) \tag{2.53}$$

Now the effective curvature energy density ρ_k^{eff} scales like a^{-2}, while the radiation energy density ρ_r scales like a^{-4}, with the scale factor a. At the Planck time $t_P = \sqrt{\frac{\hbar G}{c^5}}$ the ratio between them was many orders of magnitudes lower than 1.

$$\frac{|\rho_k^{\text{eff}}(t_P)|}{\rho_r(t_P)} \approx 10^{-62} \tag{2.54}$$

This seems unlikely since we would expect roughly the same order of magnitude for all the energy density parameters $\rho_m, \rho_r, \rho_\Lambda$, and $\rho_{\text{k}}^{\text{eff}}$. Random initial conditions would lead us to the same order of magnitude of these parameters. We also know how Ω_k scales with the scale factor.

$$\Omega_k = -\frac{k}{(aH)^2} = -\frac{k}{\dot{a}^2} \tag{2.55}$$

In the case of an inflationary GW background, the tensor power spectrum $< s(k)$ creates the GW. This is linearly related to the average GW energy density parameter (or monopole) Schulze et al. 2023.

$$\bar{\Omega}_{GW} = \frac{1}{12H_0^2 a_0^2} \frac{\eta_{eq}^2}{2\eta_0^4} P_T(k) \tag{2.56}$$

The GW created through large-scale perturbations during inflation are relevant for wavenumbers $k = 10^{-5} Mpc^{-1} - 1 Mpc^{-1}$, which corresponds to millihertz up to the Hertz range, going through both the sensitivity range of ground-based detectors, like ET Alonso et al. 2020, and space-based detectors like LISA Robson, Cornish, and Liu 2019.

2.2.3 Number Density Distribution

The `Multi_CLASS` code uses the number density of detectable GW per redshift per solid angle element from Scelfo et al. 2018:

$$\frac{d^2 N_{GW}}{dz d\Omega} = T_{obs} \frac{c\chi^2(z)}{(1+z)H(z)} R_{tot}(z) F_{GW}^{detectable}(z). \tag{2.57}$$

T_{obs} is the total observational time, $\chi(z)$ is the comoving distance, $H(z)$ is the Hubble rate, $R_{tot}(z)$ is the total comoving merger rate and $F_{GW}^{detectable}(z)$ the fraction of detectable events. For the merger rate, they include primordial black holes and binary BH (abbr) in their calculation. The authors choose the common SNR threshold $\langle \rho^2 \rangle = 8$.

$$\langle \rho^2 \rangle = \frac{1}{5} \int_{f_{min}}^{f_{max}} df \frac{h_c^2(f)}{f^2 S_n(f)} \tag{2.58}$$

For the Einstein Telescope (ET), they find that $F_{GW}^{detectable} \approx 1$ even for redshifts above 5, which have a small effect on the detection overall.

2.2.4 Projection Effects

change style, explain physics-> papers Yoo, Bonvin

For the intrinsic anisotropies, there are different contributions to the source functions Δ_l^{AGWB}. The different pertinent effects are density fluctuations, redshift space distortions, the Doppler effect and relativistic corrections or gravitational potential terms. Di Dio et al. 2013.

We write each random field as a product of the primordial curvature perturbation and a transfer function. In Dall'Armi, Ricciardone, and Bertacca 2022, they compute the different source terms using the `CLASSgal` framework. The implementation in `CLASS` follows the same framework, since `CLASSgal` has been merged into the standard public code.

$$X(\eta, \vec{k}) = T_X(\eta, \vec{k}) \zeta(\vec{k}) \tag{2.59}$$

The two-point correlation function of the curvature perturbation has the following form.

$$\langle \zeta(\vec{k}) \zeta * (\vec{k}') \rangle = (2\pi)^3 \delta(\vec{k} - \vec{k}') \frac{2\pi^2}{k^3} P(k) \tag{2.60}$$

There is one density source term, dependent on the transfer functions of matter density fluctuations $T_{\delta m}$ and of the velocity divergence of matter $T_{\theta m}$. Here, $\bar{\chi}$ is a shifted conformal time variable.

$$\bar{\chi} = \eta_0 - \eta \tag{2.61}$$

$$\Delta_\ell^{den} = \int_0^{\eta_0} d\eta W \left(b T_{\delta m} + 3 \frac{aH}{k^2} T_{\theta_m} \right) j_l(k\bar{\chi}) \tag{2.62}$$

Here, $j_l(k\bar{\chi})$ is the spherical Bessel function and we integrate over conformal time using the window function, like in the following source contributions.

The Doppler terms also depend on the velocity divergence of matter since the velocity determines the Doppler effect.

$$\Delta_\ell^{D1} = \int_0^{\eta_0} d\eta W \frac{T_{\theta_m}}{k} \left(-b_e + \frac{H'}{aH^2} + 3 \right) \frac{d}{d(k\bar{\chi})} j_l(k\bar{\chi}) \tag{2.63}$$

$$\Delta_\ell^{D2} = \int_0^{\eta_0} d\eta W T_{\theta_m}(b_e - 3)\frac{aH}{k^2} j_l(k\bar{\chi}) \tag{2.64}$$

The term for the redshift space distortions was derived by Kaiser 1987 and depends on the second derivative of the bessel function.

$$\Delta_\ell^{RSD} = \int_0^{\eta_0} d\eta W T_{\theta_m} \frac{1}{aH}\frac{d^2}{d(k\bar{\chi})^2} j_l(k\bar{\chi}) \tag{2.65}$$

There are five relativistic corrections, which can also be called gravitational potential terms since the redshift space distortions are also relativistic. In the GW case, two of these terms vanish (Dall'Armi, Ricciardone, and Bertacca 2022), while the other three are non-zero.

$$\Delta_\ell^{G1} = \int_0^{\eta_0} d\eta W T_\Psi \left(4 - b_e + \frac{H}{aH^2}\right) j_l(k\bar{\chi}) \tag{2.66}$$

$$\Delta_\ell^{G3} = \int_0^{\eta_0} d\eta W T_{\Phi'} \frac{1}{aH} j_l(k\bar{\chi}) \tag{2.67}$$

$$\Delta_\ell^{G5} = \int_0^{\eta_0} d\eta W \left(-b_e + \frac{H'}{aH^2} + 3\right) \int_0^{\tilde{\eta}} d\tilde{\eta} j_l(k\bar{\chi}) \left(T_{\Phi'}(\tilde{\eta})T_{\Psi'}(\tilde{\eta}) - \frac{1}{2}T'_{h,ij}(\tilde{\eta})n^i n^j\right) \tag{2.68}$$

In the last equation, n^i are the components of the line of sight vector.

$$\delta_{AGWB}(f_0, \hat{n}) = \int dz \tilde{W}(f_0, z)\Delta_{AGWB}(f_0, \hat{n}, z) \tag{2.69}$$

$$\begin{aligned} = \int d\bar{\chi}\tilde{W}[b(\delta_m - 3\mathcal{H}V) + (3 - b_e)\mathcal{H}V + \Psi(3 - b_e + \frac{\mathcal{H}'}{\mathcal{H}^2}) + 2I(b_e - \frac{\mathcal{H}'}{\mathcal{H}^2} - 2) \\ +(\delta a_0 + \Psi_0 - v_{\|0})(b_e - \frac{\mathcal{H}'}{\mathcal{H}^2} - 2) - v_\|(-b_e + \frac{\mathcal{H}'}{\mathcal{H}^2} + 2) \\ +\frac{1}{\mathcal{H}}\Phi' - \frac{1}{\mathcal{H}}\partial_\| v_\| - \frac{1}{2\mathcal{H}} h_{ij}^{\prime TT} n^i n^j] \end{aligned} \tag{2.70}$$

Here the following notation is used:

$$v_\| = \hat{n}\vec{v} \tag{2.71}$$

$$\partial\| = \hat{n}\vec{\nabla} \tag{2.72}$$

$$I(\bar{\chi}) = -\frac{1}{2}\int_0^{\bar{\chi}} d\tilde{\chi}(\Psi' + \Phi' - \frac{1}{2}h'_{ij})(\tilde{\chi}) \tag{2.73}$$

$$\vec{v} = \vec{\nabla}V \tag{2.74}$$

3

Frequency Dependence of the AGWB

The AGWB is not independent of the observed frequency of the GW. In the standard Multi_CLASS code, it is possible to compute the angular power spectrum of the AGWB. However, this does not include any frequency dependency of this background which can generally not be neglected, see Dall'Armi, Ricciardone, and Bertacca 2022. Therefore I added this frequency dependency which enters in two instances here. One is the frequency-dependent window function that weights contributions from different redshifts and the second is the evolution bias which accounts for new sources being added with time (i.e. lower z). Both will be discussed in detail in section 3.5 and 3.7.

We need to specify the GW frequency as a parameter in the .ini that we give to CLASS, so I implemented it as a new input parameter for Multi_CLASS.

In the standard version without frequency dependence, we can already see the influence of the different window functions and redshift ranges. *change style*

Using Multi_CLASS Bellomo et al. 2020 I plotted the GW angular power spectrum for different z, different window functions (Dirac, top hat and Gaussian) and different redshift bin widths 3.2. One of the advantages of Multi_CLASS is, that the code does not use the Limber approximation, which approximates the Bessel functions as a delta distribution.

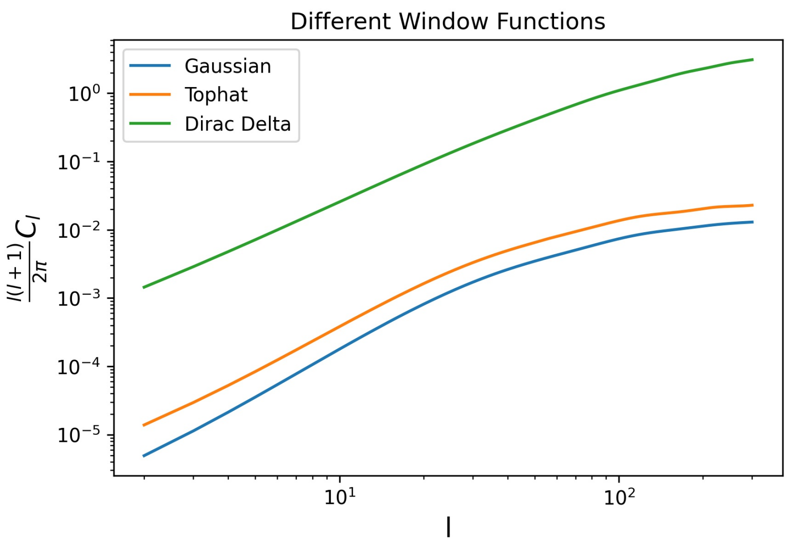

Figure 3.1: GW angular power spectrum for different window functions

As we can see in the Dall'Armi paper the window function and the evolution bias depend

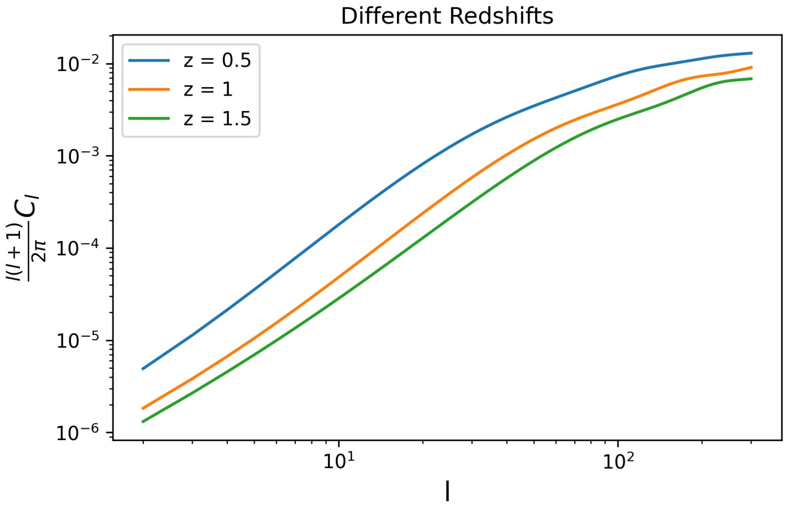

Figure 3.2: GW angular power spectrum for different redshifts

on the frequency. But this is only the case if we consider not only the inspiral phase, but also the merger and ringdown phases. For the inspiral phase only, we have the following:

$$\frac{dE_{GW}}{df_e d\Omega_e} \propto f_0^{-\frac{1}{3}}(1+z)^{-\frac{1}{3}}. \tag{3.1}$$

The window function is proportional to:

$$\tilde{W}(z) \propto \frac{f_0(E_{GW}/df_e}{\bar{\Omega}_{AGWB}(f_0)}. \tag{3.2}$$

Since we have $\bar{\Omega}_{AGWB} \propto f_0^{\frac{2}{3}}$, considering only the inspiral phase would make the window function frequency independent and thus the component separation could not work.

3.1 Energy Spectrum

For the modelling of all three phases we can use the waveform by Ajith et al. 2011:

$$A(f) = Cf_1^{-7/6}\begin{cases} f'^{-7/6}(1+\sum_{i=2}^{3}\alpha_i v^i) & f < f_1 \\ \omega_m f'^{-2/3}(1+\sum_{i=1}^{2}\epsilon_i v^i) & f_1 \leq f < f_2 \\ \omega_r \mathcal{L}(f, f_2, \sigma) & f_2 \leq f < f_3 \end{cases}$$

Note that this is the amplitude as a function of the frequency, so a Fourier transform of $A(t)$.

$$A(f) = \frac{1}{\sqrt{2\pi}}\int_{\mathbb{R}} A(t)e^{-ift}dt \tag{3.3}$$

The parameters ω_m and ω_r are used to make the function continuous. For the ringdown, we have a Lorentzian function centred around the merger to ringdown transition frequency f_2 with the width σ. The parameters α_i are post-Newtonian corrections.

The frequency f_1 at the transition of the inspiral and merger phase is the last stable orbit of the binary. Once the merger phase has started the orbits cease to be stable since

Parameter	α_2	α_3	ϵ_1	ϵ_2
Value	-323/224 + 451η/168	(27/8-11η/6)χ	1.455χ-1.890	-1.815χ + 1.656
No Spin	-323/224 + 451η/168	0	-1.890	1.656

Table 3.1: Amplitude parameters with and without the zero spin approximation.

the objects start to fall in. This frequency was calculated by Bardeen, Press, and Teukolsky 1972.

$$f_1 = \frac{c^3}{6^{3/2} 2\pi M_{tot} G} \tag{3.4}$$

The transition frequency from merger to ringdown is given by the least-damped mode (Maggiore 2008) which is also the dominant quasi-normal mode. This is part of the description of the BBH system as characterised by n normal modes with frequencies ω_n, discussed further in chapter 12.3 of the same book.

$$f_2 \approx 0.747 \frac{c}{2\pi R_S} \approx 12\mathrm{kHz} \left(\frac{\mathrm{M}_\odot}{\mathrm{M}} \right) \tag{3.5}$$

Later, we will consider the square strain as a function of frequency $|h(f)|^2$ for the energy spectrum, so we can ignore the phase $\psi(f)$.

$$h(f) = A(f) e^{-i\psi(f)} \tag{3.6}$$

Here the redshift dependence will come in through the derivation by the emission frequency, see e.g. 3.32. From this waveform template, we can get the energy spectrum in the following way.

$$\frac{dE_{GW,e}}{df_e d\Omega_e} = \frac{\pi d_L^2 c^3 f_o^2}{2G(1+z)^2} |h(f_o)|^2 \propto f_o^2 h^2(f_o) \propto h^2(t) \tag{3.7}$$

If we plot the energy spectrum as a function of z for different frequencies, see Fig. 3.4, we can see different sections of Fig. 3.3. This is because $d^2 E_{GW,e}/df_e d\Omega_e$ only depends on z through the emitted frequency. The energy spectrum is written as a function of f_e, but we implement it in such a way that the user can choose the received frequency at the detector.

$$f_e = (1+z) f_0 \tag{3.8}$$

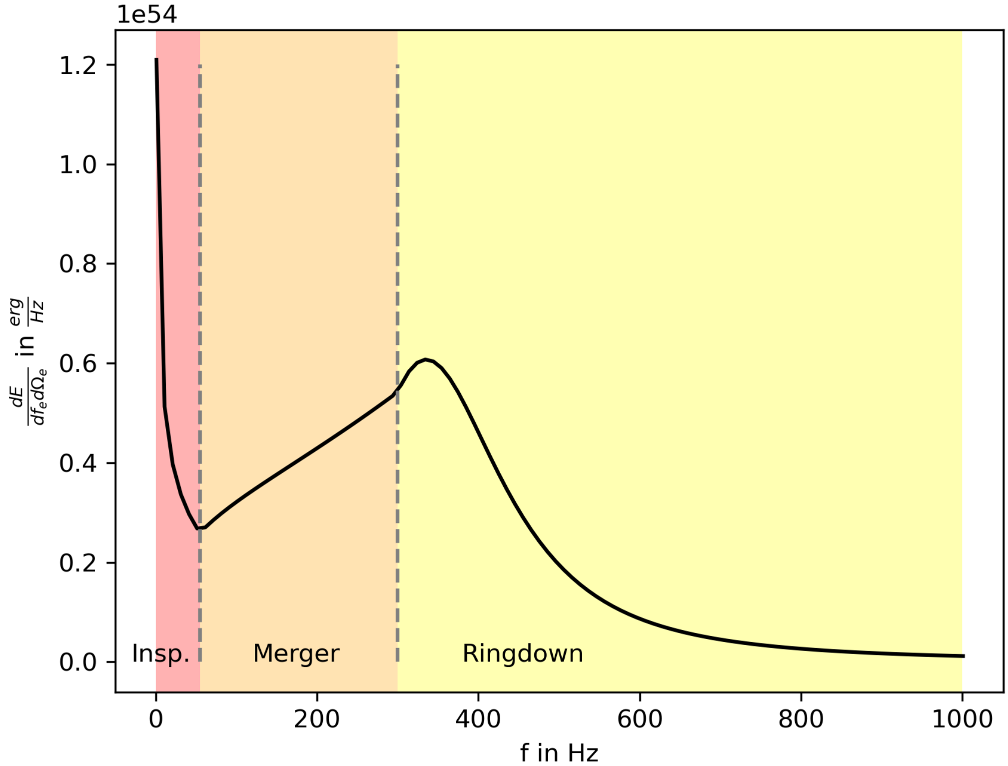

Figure 3.3: The energy spectrum as a function of frequency for a BBH merger, where both BH have a mass of $20M_{\odot}$.

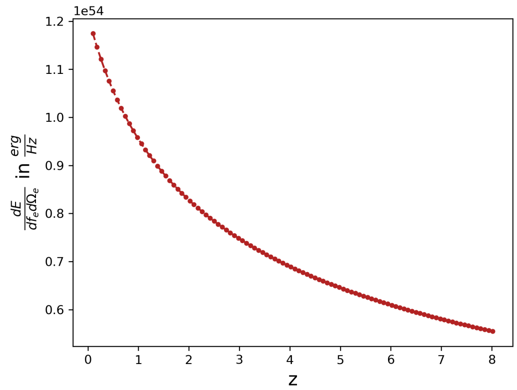

(a) The energy spectrum at an observed frequency of 1 Hz

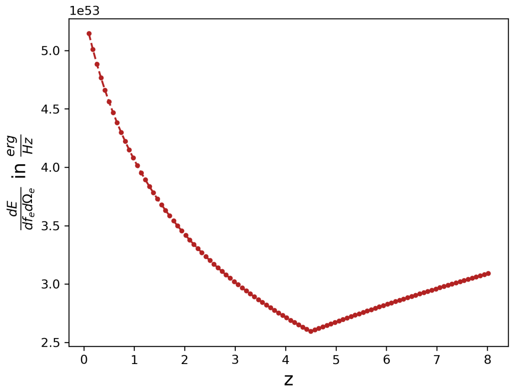

(b) The energy spectrum at an observed frequency of 10 Hz

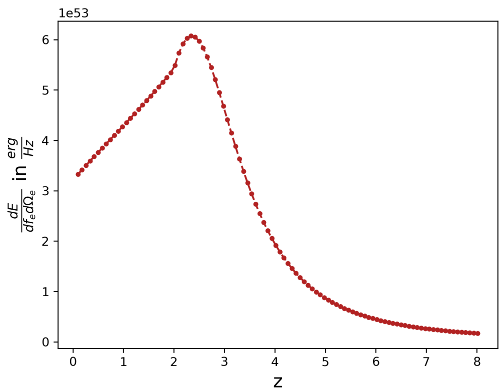

(c) The energy spectrum at an observed frequency of 100 Hz

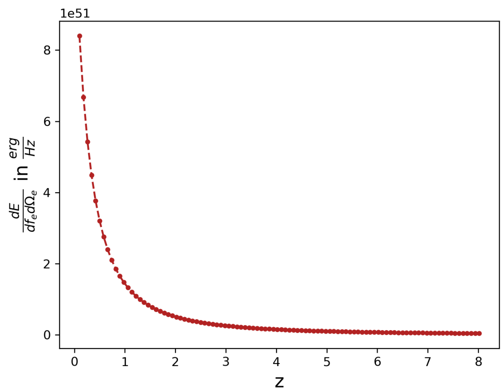

(d) The energy spectrum at an observed frequency of 1000 Hz

Figure 3.4: The energy spectrum $\frac{d^2E}{df_e d\Omega_e}$ at different observed freqeuncies as a function of redshift.

3.2 Star Formation Rate

3.2.1 UniverseMachine

For the star formation rate, we use the UniverseMachine code from Behroozi et al. 2019. They use observational constraints and data from simulations to compute SFR for individual galaxies.

In the ΛCDM cosmology, galaxies form at the centre of haloes. Haloes are gravitationally self-bound structures that contain virialised dark matter. This means that the virial equation applies in this case. Here, T is the potential energy and U is the kinetic energy.

$$2T = U \tag{3.9}$$

So far, there exists no framework in which we can derive the SFR from first principles. This is why the authors use a double power law plus Gaussian and determine the best-fit parameters for this functional form. This determines the SFR for every halo at a given redshift. They use weak priors and observational constraints for less bias and the potential to reveal new physics.

Dark matter simulations, here Bolshoi-Planck [A. A. Klypin, Trujillo-Gomez, and Primack 2011] and MultiDark Planck 2 (MDPL2) A. Klypin et al. 2016, are used, which simulate a mock universe. They contain halo merger trees, which can be compared to observations. Behroozi et al. used data from multiple experiments, such as the Sloan Digital Sky Survey (SDSS) Abazajian et al. 2009, Ultravista McCracken et al. 2012. The observables include stellar mass functions, UV luminosity functions and galaxy auto-correlation functions. Using this data, they compute a likelihood and run a Markov Chain Monte Carlo (MCMC) algorithm to sample the SFR range.

Like in Dall'Armi, Ricciardone, and Bertacca 2022 we consider only star-forming galaxies. This could be modified in a future version of the code by including the fraction of quenched galaxies $f_Q = 1 - f_{SF}$, which could be taken from the UniverseMachine paper as well. The adopted SFR functional form is the following.

$$SFR_{SF} = \epsilon \left[\left(v^{\alpha} + v^{\beta} \right)^{-1} + \gamma \exp\left(-\frac{\log_{10}(v)^2}{2\delta^2} \right) \right] \tag{3.10}$$

The characteristic SFR in $M_{\odot}\ yr^{-1}$ is the global factor ϵ. For the slope of the $SFR - v_{Mpeak}$ relation, we have a faint-end and a massive-end slope parameter α and β, respectively. This is because $v_{Mpeak} \propto M_h^3$ 3.18, so a higher velocity at the peak mass corresponds to a higher halo mass. Furthermore, γ is the strength and δ the width of the Gaussian SFR efficiency boost.

The velocity v is defined as the ratio of the real (v_{Mpeak}) and the characteristic (V) velocity at the halo peak mass, both in kms^{-1}.

$$v = \frac{v_{Mpeak}}{V \cdot kms^{-1}} \tag{3.11}$$

The other parameters, except for δ, scale differently for different redshift regions. For V, ϵ and α, the scaling is separated into $z = 0$, $z \approx 1-2$, $z = 3-7$ and $z > 7$. The parameters β and γ have three scaling regions instead of four, as they are not well constrained at high redshifts.

$$\log_{10}(V) = V_0 + V_a(1-a) + V_{la} ln(1+z) + V_z z \tag{3.12}$$

$$\log_{10}(\epsilon) = \epsilon_0 + \epsilon_a(1-a) + \epsilon_{la} ln(1+z) + \epsilon_z z \tag{3.13}$$

$$\alpha = \alpha_0 + \alpha_a(1-a) + \alpha_{la} ln(1+z) + \alpha_z z \tag{3.14}$$

$$\beta = \beta_0 + \beta_a(1-a) + \beta_z z \tag{3.15}$$

$$\log_{10}(\gamma) = \gamma_0 + \gamma_a(1-a) + \gamma_{la} ln(1+z) + \gamma_z z \tag{3.16}$$

$$\delta = \delta_0 \tag{3.17}$$

The median v_{Mpeak} is taken from the *Bolshoi-Planck* DM simulation as

$$v_{Mpeak}(M_h, a) = 200 \frac{km}{s} \left[\frac{M_h}{M_{200kms}(a)} \right]^3 \tag{3.18}$$

$$M_{200kms}(a) = \frac{1.64 \cdot 10^{12} M_\odot}{()\frac{a}{0.378})^{-0.142} + (\frac{a}{0.378})^{-1.79}}. \tag{3.19}$$

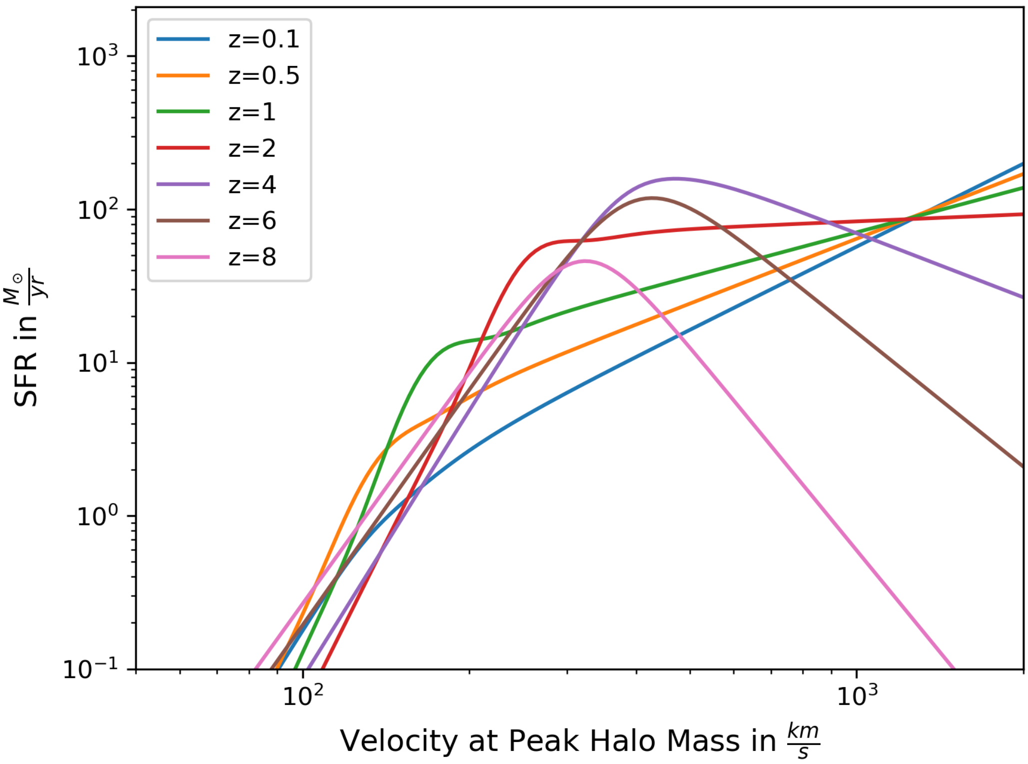

Figure 3.5: SFR for star-forming galaxies for different redshifts. The velocity at the historical peak halo mass corresponds to the standard halo mass, see equation 3.18.

3.3 Halo Mass Function

The merger rate of BBH depends on the number of haloes since their formation takes place in haloes. This is why it depends on the halo mass function $\frac{dn}{dM_h}(z_f, M_h)$ integrated over the halo mass.

$$R_{BBH}(z) \propto \int dM_h \frac{dn}{dM_h}(z_f, M_h) \langle SFR(M_h, z_f) \rangle_{SF} \tag{3.20}$$

We first consider the variance of the matter density field σ^2 which we get from the linear matter power spectrum integrated over the wavenumber k with a tophat window function of the radius R.

$$\sigma^2(R, z) = \int_0^\infty k^2 P_{lin}(k, z) W^2(k, R) dk \tag{3.21}$$

For a spherical halo model, we get the radius through the mass and the density.

$$R = \sqrt[3]{\frac{3M}{4\pi\rho_m}} \tag{3.22}$$

Then, the halo mass function comes from the logarithmic derivative of σ^{-1} by the halo mass.

$$\frac{dn(M)}{dM} = \frac{\rho_m}{M^2} \frac{d\ln(\frac{1}{\sigma})}{d\ln M} f_{NL}(\sigma) \tag{3.23}$$

The factor f_{NL} accounts for non-linear effects in the halo collapse. There are different ways to model these effects. A common analytical one is the Press-Schechter formalism parametrised by the critical overdensity δ_c.

$$\delta = \frac{\delta\rho}{\bar{\rho}} \tag{3.24}$$

$$f_{PS}(\sigma) = \sqrt{\frac{2}{\pi}} \frac{\delta_c}{\sigma} \exp(-\frac{\delta_c^2}{2\sigma^2}) \tag{3.25}$$

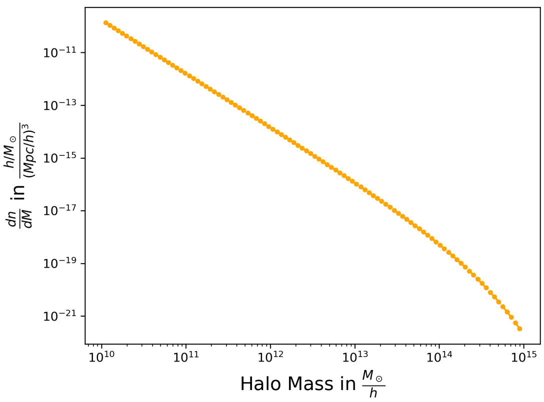

(a) The halo mass function in units of $\frac{h/M_\odot}{(Mpc/h)^3}$ or respectively $\frac{h^4}{M\odot Mpc^3}$

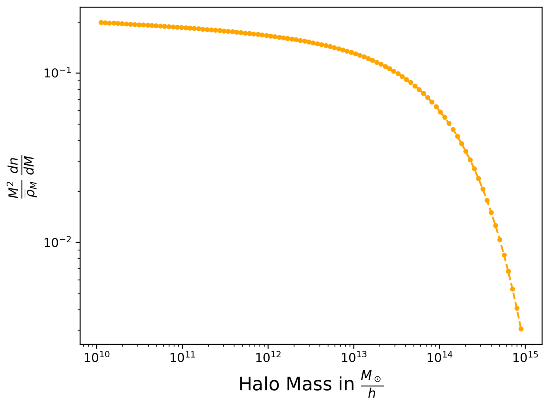

(b) The dimensionless halo mass function

Figure 3.6: Plots of the used HMFs.

3.4 Merger Rate

$$R_{BBH}(z = 0) = 19\,\text{Gpc}^{-3}\text{yr}{-1} \tag{3.26}$$

$$R_{BBH}(z) = \mathcal{A}_{LIGO}^{BBH} \int dt_d p(t_d) \int dM_h \frac{dn}{dM_h}(z_f, M_h) \langle SFR(M_h, z_f) \rangle_{SF} \tag{3.27}$$

Here, we have the time delay distribution $p(t_d)$, where the time delay is between the formation and the merger of the binary. (physical explanation)

For the merger rate of binary black holes, we need the star formation rate.

...

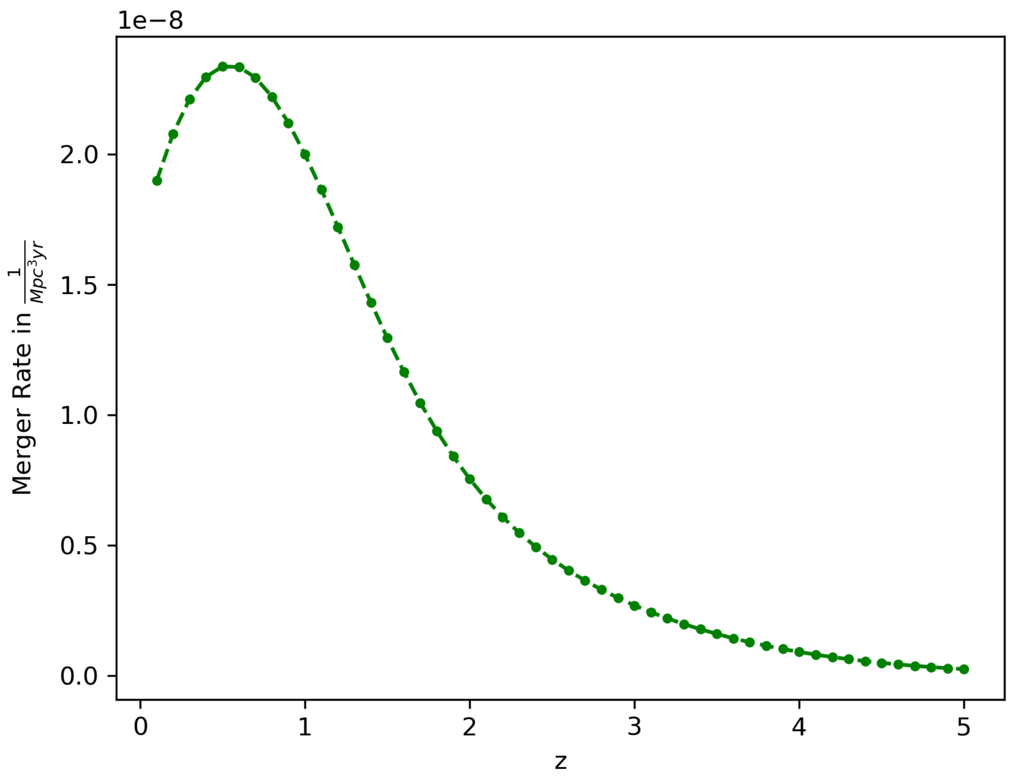

Figure 3.7: BBH merger rate as a function of the redshift z

3.5 Window Function

In Dall'Armi et al. Dall'Armi, Ricciardone, and Bertacca 2022 we see that the frequency dependence of the dipole comes from the evolution bias and the window function. The evolution bias accounts for the fact that more sources are created with time. The window function is used when we integrate the source functions over the redshift.

$$\delta_{AGWB}(f_0, \hat{n}) = \int dz \tilde{W}(f_0, z) \Delta_{AGWB}(f_0, \hat{n}, z) \tag{3.28}$$

We can then Fourier and Legendre transform the GW density contrast:

$$\delta_X(f_0, \vec{k}) = \int \frac{d^3\vec{x}}{(2\pi)^{\frac{3}{2}}} \delta_X(f_0, \vec{x}) \tag{3.29}$$

$$\Delta_l(k, f_0) = \int d\phi \int d\mu \mathcal{P}_l(\mu) \delta(\vec{k}, f_0) \tag{3.30}$$

From that, we can calculate the angular power spectrum using the primordial power spectrum:

$$C_l = 4\pi \int \frac{dk}{k} P(k) \Delta_l \Delta_l^* \tag{3.31}$$

Here, X and Y can be the intrinsic, shot noise or kinematic (dipole) contribution. Note, that this Δ is not the same as in equation 2.69.

The window function depends upon others on the binary black hole merger rate.

$$\tilde{W}(z, f_0) = \frac{f_0}{\rho_c c^2 \bar{\Omega}_{AGWB}(f_0)} \frac{R_{BBH}(z)}{(1+z)H(z)} \frac{dE_{GW}}{df_e d\Omega_e}(f_e)\bigg|_{f_e=(1+z)f_0} \tag{3.32}$$

The window function is normalised using the monopole, which is the same expression integrated over z.

$$\bar{\Omega}_{AGWB}(f_0) = \frac{f_0}{\rho_c} \frac{d\rho_{GW}}{df} \tag{3.33}$$

$$= \frac{f_0}{\rho_c c^2} \int \frac{dz}{(1+z)H(z)} R_{BBH}(z) \frac{dE_{GW}}{df_e d\Omega_e}(f_e) \tag{3.34}$$

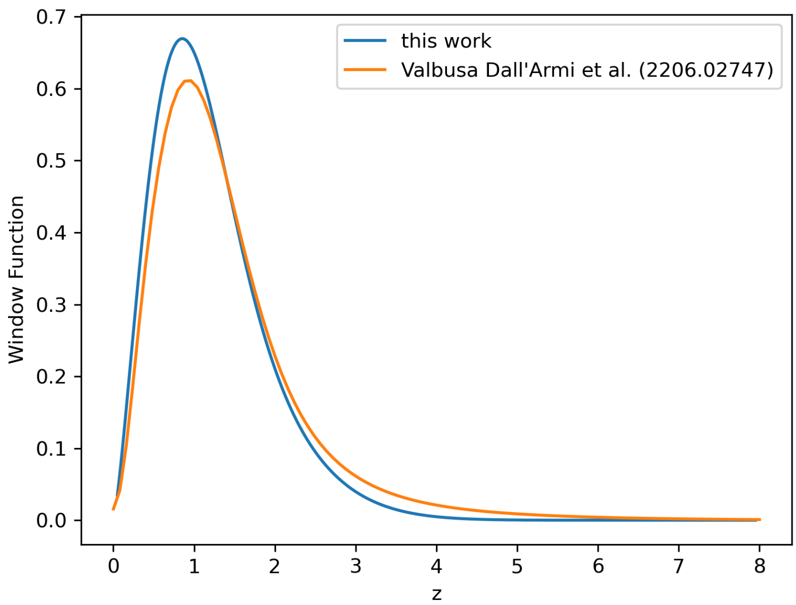

Figure 3.8: The final window function at 1 Hertz for this code in blue for comparison with Dall'Armi, Ricciardone, and Bertacca 2022 in orange.

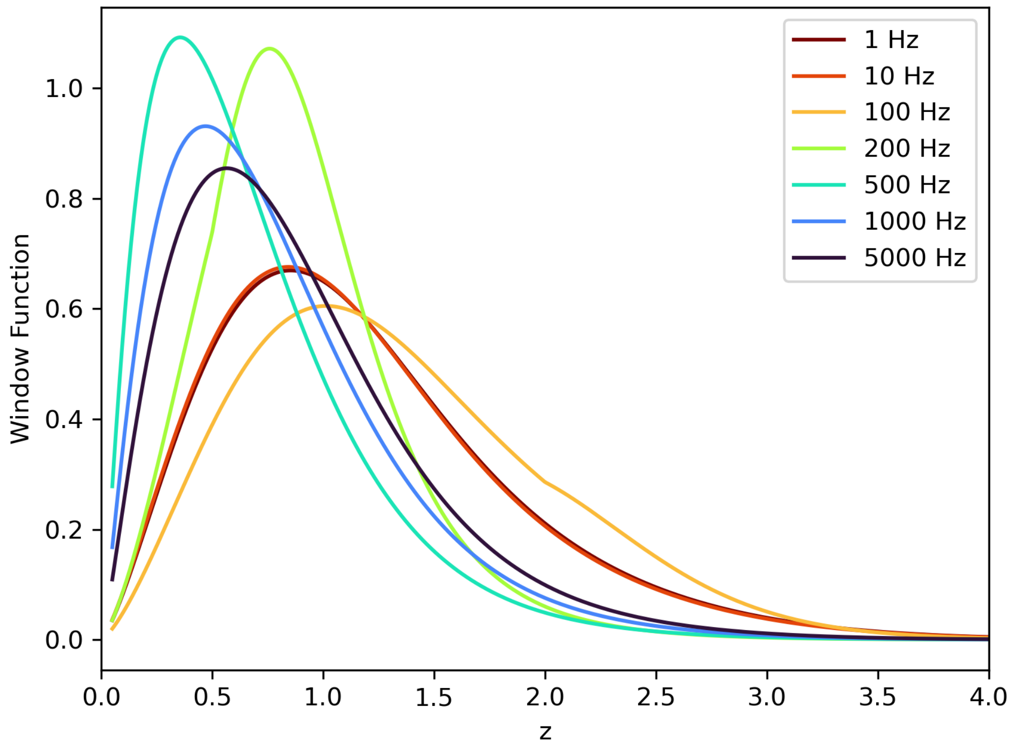

Figure 3.9: The window functions at different observed frequencies.

3.6 Bias & Magnification Bias

change style

If one compares the contributions to Δ_l^{AGWB} between `CLASSgal` and the Dall'Armi paper Dall'Armi, Ricciardone, and Bertacca 2022, the magnification bias has to be $s = \frac{2}{5}$ for the expressions to match. To find out why this is the case, I tried some calculations with $\frac{dN}{dz}$, but could not match this value. After reading the paper by Bertacca et al. Bertacca et al. 2020 (recommended by Lorenzo), one can see that they derive their expressions from first principles without introducing the magnification bias separately.

3.7 Evolution Bias

The evolution bias accounts for the creation of new sources. This is why it depends on the redshift derivative of the merger rate and the energy spectrum of one merger. We can write this in terms of the derivative of the GW energy flux of the scale factor a.

$$b_e(f_0, z) = \frac{d\ln(F)}{d\ln(a)}(f_0, z) \tag{3.35}$$

$$= -\frac{1+z}{F(f_0, z)}\frac{dF}{dz}(f_0, z) \tag{3.36}$$

The energy flux of GW is a product of the energy spectrum of one binary, using the waveform by Ajith et al. Ajith et al. 2011 and the merger rate of binary black holes as a function of redshift.

$$F(f_0, z) = R_{BBH}(z) \frac{dE_{GW}}{df_e d\Omega_e}(f_0, z) \tag{3.37}$$

It makes sense to use an Einstein-Boltzmann solver, like CLASS (cite), since the formalism of computing the angular power spectrum is similar to doing this for galaxy counts.

4

Component Separation Methods

4.1 Instrumental Noise

Currently, the main problem in extracting the GW background is the high instrumental noise.

4.1.1 LIGO, Virgo & KAGRA

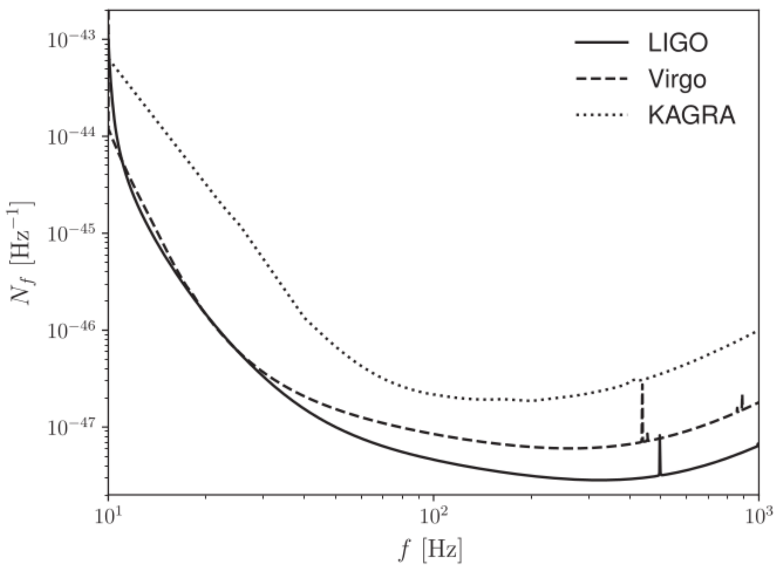

Figure 4.1: Design sensitivity curves for the LVK detector network. For LIGO, this is the advanced LIGO A+ design sensitivity and for Virgo the O5 sensitivity.

As can be seen in Fig.4.2, using cross-correlations between the ground-based detectors improves the sensitivity, especially at higher multipoles. Adding auto-correlations of the detectors mostly influences $\ell = 2$, which is due to the L-shaped geometry of the detectors.

4.1.2 Einstein Telescope & Cosmic Explorer

The planned ground-based detectors Einstein Telescope (ET) and Cosmic Explorer (CE) will improve the sensitivity by 1-2 orders of magnitude, see Fig.4.3.

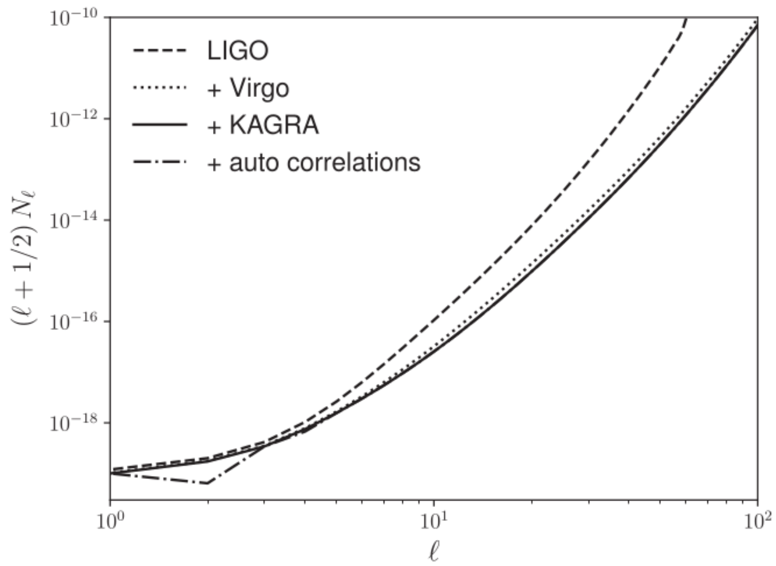

Figure 4.2: The noise angular power spectrum for LVK.

Using the cross-correlations between ET and CE, see Fig.4.4, the noise angular power spectrum is expected to drop from 10^{-19} to $\approx 6 \cdot 10^{-24}$ for the dipole $\ell = 1$. Here again, the improvement coming from the auto-correlation is due to the detector shape.

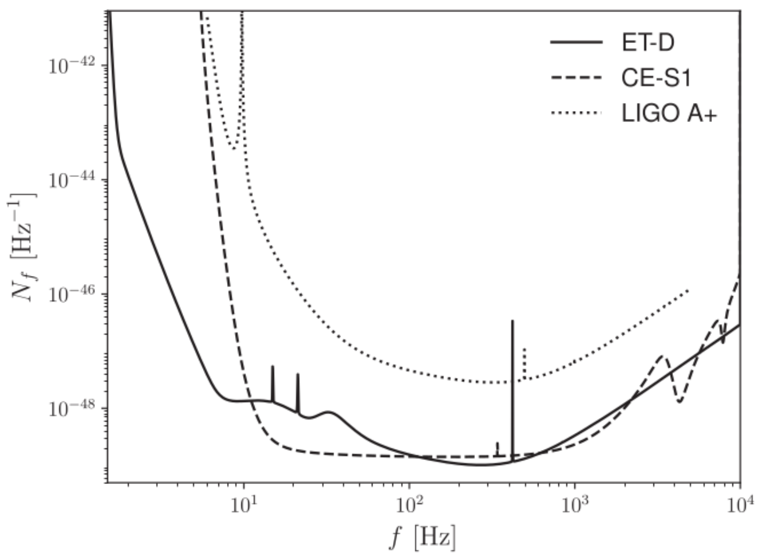

Figure 4.3: The design sensitivity curve for ET and CE compared to LIGO A+.

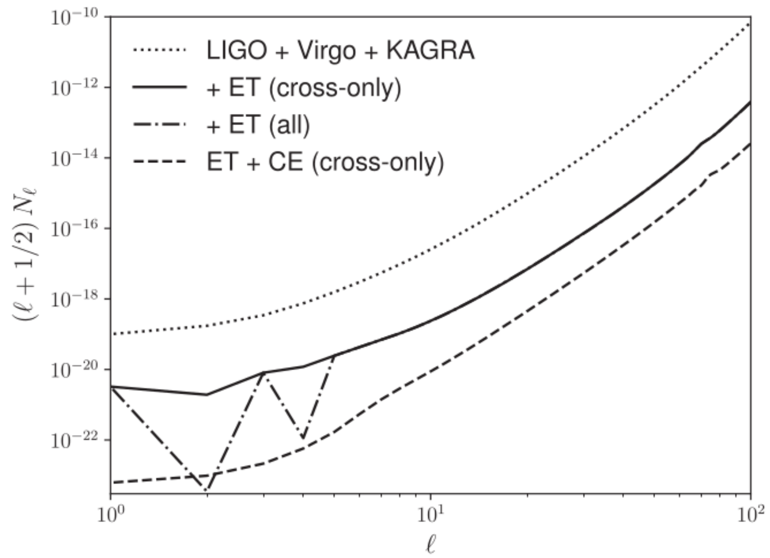

Figure 4.4: SFR for star-forming galaxies for different redshifts. The velocity at the historical peak halo mass corresponds to the standard halo mass, see equation 3.18.

4.2 Internal Linear Combination?

Lorenzo's paper, why we can't use it

5

Information Field Theory

Since the noise in GW detectors is very high, especially compared to the GW background, it makes sense to use powerful methods to separate the signal from the noise. One promising method is information field theory (IFT).
change style:
Dr Torsten Enßlin from the Max Planck Institute in Garching gave a lecture about information field theory (IFT) in 2022. From that script, I read chapters 6 through 11. I also watched his talk, where he applied IFT to different problems, like the tomography of the Milky Way. The idea is to use Bayesian statistics to reconstruct a signal from data which contains noise. His group also developed a Python package, called nifty, which we can use. This can also be used on the gravitational wave background as a tool to separate it from shot noise.

Information field theory is a technique for signal reconstruction and field inference designed by Torsten Enßlin and his group at the Max Planck Institute in Garching. Its goal is to use a formalism similar to the one used in Quantum Field Theory to be able to reuse methods to infer fields from data. The problem at the base is, that we want to infer a spatially continuously distributed field from a finite amount of data. To do that, we can add our knowledge about physical laws, statistics, etc. of the problem, in the form of correlation functions.

We need to define our probability density functions over the space of all possibilities, which is why we will integrate using path integrals in this formalism.

If we assume a linear measurement, our data consists of the signal modified by a response function and added noise.

$$d = Rs + n \tag{5.1}$$

$$(Rs)_i = \int dx R_{ix} s_x \tag{5.2}$$

The response corresponds to the point spread function of our instrument and other linear operations performed on the data.

With Gaussian noise, we get the following likelihood:

$$P(d|s) = \mathcal{N}(d - Rs, N). \tag{5.3}$$

5.1 Information Hamiltonian

Using Bayes theorem, we define what is called an information Hamiltonian.

$$P(s|d) = \frac{P(d|s)P(s)}{P(d)} \tag{5.4}$$

$$= \frac{e^{-\mathcal{H}(d,s)}}{Z_d} \tag{5.5}$$

Here, Z_d is the partition function, which is the evidence here.

$$Z_d = P(d) \tag{5.6}$$

$$\mathcal{H}(d,s) = -ln(P(d|s)) - ln(P(s)) \tag{5.7}$$

5.2 Wiener Filter

For a Gaussian prior and a Gaussian signal, we obtain the following Hamiltonian.

$$\mathcal{H}(d,s) = \frac{1}{2}(d - Rs)^{\dagger}N^{-1}(d - Rs) + \frac{1}{2}s^{\dagger}S^{-1}s \tag{5.8}$$

With quadratic completion, we can rewrite this in canonical form.

$$\mathcal{H}(d,s) = \frac{1}{2}(s - m)^{\dagger}D^{-1}(s - m) \tag{5.9}$$

When applying the covariance to the source, we get the mean according to the Wiener filter.

$$m = Dj \tag{5.10}$$

$$D = (S^{-1} + R^{\dagger}N^{-1}R)^{-1} \tag{5.11}$$

$$j = R^{\dagger}N^{-1}d \tag{5.12}$$

The covariance can also be written with the signal and the mean:

$$D = \langle (s - m)(s - m)^{\dagger} \rangle_{s|d} \tag{5.13}$$

Then, the posterior of the Wiener filter is a Gaussian distribution with mean $s - m$ and the earlier-mentioned covariance.

$$P(s|d) = \mathcal{N}(s - m, D) \tag{5.14}$$

6

Results

To get a frequency-dependent angular power spectrum from `Multi_CLASS`, we implemented a frequency-dependent window function (see 3.5) and evolution bias (see 3.7). Using this, we can choose a measured GW frequency as an input parameter and compute the angular power spectrum.

We then extended the `CLASS` code to also include the dipole l=1, which I also changed in `Multi_CLASS`.

6.1 Frequency Dependent AGWB Angular Power Spectrum

6.2 AGWB vs. Noise

For the noise angular power spectrum, we assume Gaussian noise using the best anisotropic noise sensitivity for ET and CE using cross-correlations (at $l = 1$). This is a very optimistic assumption. The computed C_l used for the separation reach up to $l = 30$. Looking at Fig. 4.4, our assumed noise curve would have the shape of $l + \frac{1}{2}$ up to $l = 30$, which would increase more slowly than the actual sensitivity curve.

6.2.1 1D Toy Model

6.2.2 Sky Map

6.3 CGWB vs. Noise

6.3.1 Sky Map

7

Conclusion & Outlook

We compute the angular power spectra of the AGWB using `MultiCLASS` with a dependence on the measured frequency. We then use this result for an IFT separation with the NIFTy package.

For the noise power spectrum, we optimistically assume Gaussian noise. This could be made more realistic by using the ET spectrum directly for the separation.

In the future, it would be natural to extend this and use the frequency dependence directly in NIFTy. This should improve the separation since it is an extra dimension that can be used to perform the separation.

List of Figures

Acknowledgements

I would like to thank my supervisors Prof. Dr. Philipp Mertsch and Prof. Dr. Julien Lesgourgues. Lorenzo Vallbusa Dal'Armi also offered his expertise on gravitational waves and kindly provided some of his data to compare with my code. Additionally, Sefa Pamuk, Tobias Thrien and Christian Radermacher were always happy to discuss physical concepts and provide help regarding the CLASS code. Laurin Söding helped me with some concerns regarding the NIFTy code, as well. Lastly, thanks to Clemens Panitz and Sefa Pamuk? for proofreading this thesis.

Bibliography

Agazie, Gabriella et al. (June 28, 2023). *The NANOGrav 15-year Data Set: Evidence for a Gravitational-Wave Background*. DOI: 10.3847/2041-8213/acdac6. arXiv: 2306.16213[astro-ph,physics:gr-qc]. URL: http://arxiv.org/abs/2306.16213 (visited on 09/15/2023).

Holten, J. W. van (Mar. 2019). "Gravitational waves from generalized newtonian sources". In: *Fortschritte der Physik* 67.3, p. 1800083. ISSN: 00158208. DOI: 10.1002/prop.201800083. arXiv: 1809.05670[astro-ph,physics:gr-qc]. URL: http://arxiv.org/abs/1809.05670 (visited on 09/11/2023).

Collaboration, The LIGO Scientific et al. (Feb. 23, 2022). *The population of merging compact binaries inferred using gravitational waves through GWTC-3*. arXiv: 2111.03634[astro-ph,physics:gr-qc]. URL: http://arxiv.org/abs/2111.03634 (visited on 10/04/2023).

Capurri, Giulia et al. (Nov. 1, 2021). "Intensity and anisotropies of the stochastic Gravitational Wave background from merging compact binaries in galaxies". In: *Journal of Cosmology and Astroparticle Physics* 2021.11, p. 032. ISSN: 1475-7516. DOI: 10.1088/1475-7516/2021/11/032. arXiv: 2103.12037[astro-ph,physics:gr-qc]. URL: http://arxiv.org/abs/2103.12037 (visited on 09/22/2023).

Abbott, B. P. et al. (Feb. 11, 2016). "Observation of Gravitational Waves from a Binary Black Hole Merger". In: *Physical Review Letters* 116.6, p. 061102. ISSN: 0031-9007, 1079-7114. DOI: 10.1103/PhysRevLett.116.061102. URL: https://link.aps.org/doi/10.1103/PhysRevLett.116.061102 (visited on 09/01/2023).

Christensen, Nelson (Jan. 1, 2019). "Stochastic gravitational wave backgrounds". In: *Reports on Progress in Physics* 82.1, p. 016903. ISSN: 0034-4885, 1361-6633. DOI: 10.1088/1361-6633/aae6b5. URL: https://iopscience.iop.org/article/10.1088/1361-6633/aae6b5 (visited on 08/10/2023).

Phinney, E. S. (Aug. 1, 2001). *A Practical Theorem on Gravitational Wave Backgrounds*. arXiv: astro-ph/0108028. URL: http://arxiv.org/abs/astro-ph/0108028 (visited on 09/15/2023).

Schulze, Florian et al. (May 2, 2023). *GW_CLASS: Cosmological Gravitational Wave Background in the Cosmic Linear Anisotropy Solving System*. arXiv: 2305.01602[astro-ph,physics:gr-qc]. URL: http://arxiv.org/abs/2305.01602 (visited on 08/10/2023).

Blas, Diego, Julien Lesgourgues, and Thomas Tram (July 1, 2011). "The Cosmic Linear Anisotropy Solving System (CLASS) II: Approximation schemes". In: *Journal of Cosmology and Astroparticle Physics* 2011.7, pp. 034–034. ISSN: 1475-7516. DOI: 10.1088/1475-7516/2011/07/034. arXiv: 1104.2933[astro-ph]. URL: http://arxiv.org/abs/1104.2933 (visited on 09/15/2023).

Alonso, David et al. (June 22, 2020). "Noise angular power spectrum of gravitational wave background experiments". In: *Physical Review D* 101.12, p. 124048. ISSN: 2470-0010, 2470-0029. DOI: 10.1103/PhysRevD.101.124048. URL: https://link.aps.org/doi/10.1103/PhysRevD.101.124048 (visited on 08/10/2023).

Robson, Travis, Neil Cornish, and Chang Liu (May 23, 2019). “The construction and use of LISA sensitivity curves”. In: *Classical and Quantum Gravity* 36.10, p. 105011. ISSN: 0264-9381, 1361-6382. DOI: 10.1088/1361-6382/ab1101. arXiv: 1803.01944[astro-ph,physics:gr-qc]. URL: http://arxiv.org/abs/1803.01944 (visited on 09/22/2023).

Scelfo, Giulio et al. (Sept. 25, 2018). “GW$\times$LSS: Chasing the Progenitors of Merging Binary Black Holes”. In: *Journal of Cosmology and Astroparticle Physics* 2018.9, pp. 039–039. ISSN: 1475-7516. DOI: 10.1088/1475-7516/2018/09/039. arXiv: 1809.03528[astro-ph,physics:gr-qc]. URL: http://arxiv.org/abs/1809.03528 (visited on 08/10/2023).

Di Dio, Enea et al. (Nov. 20, 2013). “The CLASSgal code for Relativistic Cosmological Large Scale Structure”. In: *Journal of Cosmology and Astroparticle Physics* 2013.11, pp. 044–044. ISSN: 1475-7516. DOI: 10.1088/1475-7516/2013/11/044. arXiv: 1307.1459[astro-ph]. URL: http://arxiv.org/abs/1307.1459 (visited on 08/09/2023).

Dall’Armi, Lorenzo Valbusa, Angelo Ricciardone, and Daniele Bertacca (Nov. 1, 2022). “The Dipole of the Astrophysical Gravitational-Wave Background”. In: *Journal of Cosmology and Astroparticle Physics* 2022.11, p. 040. ISSN: 1475-7516. DOI: 10.1088/1475-7516/2022/11/040. arXiv: 2206.02747[astro-ph,physics:gr-qc]. URL: http://arxiv.org/abs/2206.02747 (visited on 02/06/2023).

Kaiser, Nick (July 1987). “Clustering in real space and in redshift space”. In: *Monthly Notices of the Royal Astronomical Society* 227.1, pp. 1–21. ISSN: 0035-8711, 1365-2966. DOI: 10.1093/mnras/227.1.1. URL: https://academic.oup.com/mnras/article-lookup/doi/10.1093/mnras/227.1.1 (visited on 10/02/2023).

Bellomo, Nicola et al. (Oct. 6, 2020). “Beware of commonly used approximations I: errors in forecasts”. In: *Journal of Cosmology and Astroparticle Physics* 2020.10, pp. 016–016. ISSN: 1475-7516. DOI: 10.1088/1475-7516/2020/10/016. arXiv: 2005.10384[astro-ph]. URL: http://arxiv.org/abs/2005.10384 (visited on 08/10/2023).

Ajith, P. et al. (June 15, 2011). “Inspiral-merger-ringdown waveforms for black-hole binaries with non-precessing spins”. In: *Physical Review Letters* 106.24, p. 241101. ISSN: 0031-9007, 1079-7114. DOI: 10.1103/PhysRevLett.106.241101. arXiv: 0909.2867[astro-ph,physics:gr-qc]. URL: http://arxiv.org/abs/0909.2867 (visited on 02/06/2023).

Bardeen, James M., William H. Press, and Saul A. Teukolsky (Dec. 1972). “Rotating Black Holes: Locally Nonrotating Frames, Energy Extraction, and Scalar Synchrotron Radiation”. In: *The Astrophysical Journal* 178, p. 347. ISSN: 0004-637X, 1538-4357. DOI: 10.1086/151796. URL: http://adsabs.harvard.edu/doi/10.1086/151796 (visited on 10/03/2023).

Maggiore, Michele (2008). *Gravitational waves*. OCLC: 262833538. Oxford: Oxford University Press. ISBN: 978-0-19-171766-6.

Behroozi, Peter et al. (Sept. 21, 2019). “UniverseMachine: The Correlation between Galaxy Growth and Dark Matter Halo Assembly from z=0-10”. In: *Monthly Notices of the Royal Astronomical Society* 488.3, pp. 3143–3194. ISSN: 0035-8711, 1365-2966. DOI: 10.1093/mnras/stz1182. arXiv: 1806.07893[astro-ph]. URL: http://arxiv.org/abs/1806.07893 (visited on 02/06/2023).

Klypin, Anatoly A., Sebastian Trujillo-Gomez, and Joel Primack (Oct. 20, 2011). “DARK MATTER HALOS IN THE STANDARD COSMOLOGICAL MODEL: RESULTS FROM THE BOLSHOI SIMULATION”. In: *The Astrophysical Journal* 740.2, p. 102. ISSN: 0004-637X, 1538-4357. DOI: 10.1088/0004-637X/740/2/102. URL: https://iopscience.iop.org/article/10.1088/0004-637X/740/2/102 (visited on 10/02/2023).

Klypin, Anatoly et al. (Apr. 21, 2016). “MultiDark simulations: the story of dark matter halo concentrations and density profiles”. In: *Monthly Notices of the Royal Astronomical Society* 457.4, pp. 4340–4359. ISSN: 0035-8711, 1365-2966. DOI: 10.1093/mnras/stw248.

URL: https://academic.oup.com/mnras/article-lookup/doi/10.1093/mnras/stw248 (visited on 10/02/2023).

Abazajian, Kevork N. et al. (June 1, 2009). "THE SEVENTH DATA RELEASE OF THE SLOAN DIGITAL SKY SURVEY". In: *The Astrophysical Journal Supplement Series* 182.2, pp. 543–558. ISSN: 0067-0049, 1538-4365. DOI: 10.1088/0067-0049/182/2/543. URL: https://iopscience.iop.org/article/10.1088/0067-0049/182/2/543 (visited on 10/02/2023).

McCracken, H. J. et al. (Aug. 2012). "UltraVISTA: a new ultra-deep near-infrared survey in COSMOS". In: *Astronomy & Astrophysics* 544, A156. ISSN: 0004-6361, 1432-0746. DOI: 10.1051/0004-6361/201219507. URL: http://www.aanda.org/10.1051/0004-6361/201219507 (visited on 10/02/2023).

Bertacca, Daniele et al. (May 11, 2020). "Projection effects on the observed angular spectrum of the astrophysical stochastic gravitational wave background". In: *Physical Review D* 101.10, p. 103513. ISSN: 2470-0010, 2470-0029. DOI: 10.1103/PhysRevD.101.103513. arXiv: 1909.11627[astro-ph,physics:gr-qc]. URL: http://arxiv.org/abs/1909.11627 (visited on 08/10/2023).